Journal of Materials Chemistry A

Accepted Manuscript

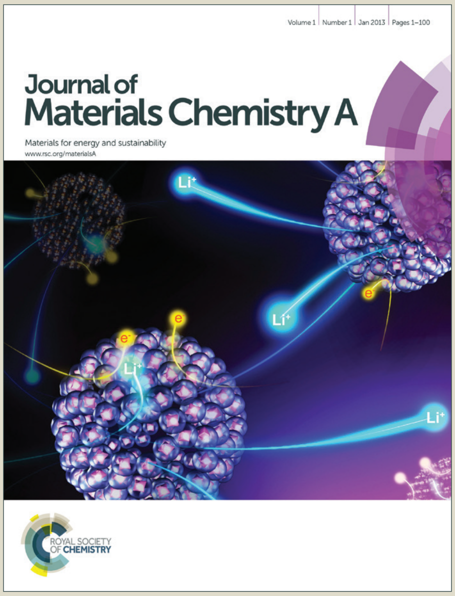

ROYAL SOCIETY OF CHEMISTRY

www.rsc.org/materialsA

A facile general strategy for synthesis of palladium-based bimetallic alloyed nanodendrites with enhanced electrocatalytic performance for methanol and ethylene glycol oxidation

Jie-Ning Zheng, Li-Li He, Fang-Yi Chen, Ai-Jun Wang,* Meng-Wei Xue, Jiu-Ju Feng*

College of Chemistry and Life Science, College of Geography and Environmental Science, Zhejiang Normal University, Jinhua, 321004, China

**Corresponding author: jjfeng@zjnu.cn (JJF), ajwang@zjnu.cn (AJW).*

Abstract

In this work, a facile general strategy is developed for preparation of palladium-based bimetallic alloyed nanodendrites (PdM NDs, M = Pt, Co, and Ni) via coreduction of Pd (II) acetylacetonate and M (II/III) acetylacetonate salts with oleylamine. Hexadecylpyridinium chloride monohydrate (HDPC) is used as a co-surfactant for further preventing the nanodendrites from aggregation. Control experiments by varying the precursors and reaction time demonstrate that the dendritic nanocrystals are formed via the aggregation-based crystal growth. The as-prepared hybrid nanocrystals display the improved electrocatalytic activity and better stability for methanol and ethylene glycol (EG) oxidation, compared with home-made Pd NDs and commercial Pd black catalysts. The developed method provides a novel platform for synthesis of novel electrocatalysts in fuel cells.

Keywords: Nanodendrites; Alloys; Oleylamine; Methanol; Ethylene glycol

1. Introduction

During the last several decades, noble metals (e.g. Pt, Pd, Au, and Ag) have attracted great research attention, owing to their excellent catalytic, electronic, photonic and sensing properties.[1-4] However, their sky-rocketing price is a major obstacle for their commercial applications. To enhance the mass activity of metallic nanocrystals and thereby reduce their usage in electronic devices, many efforts have been devoted to adjusting their composition,[5, 6] size [7, 8] and morphology,[9, 10] and found that their morphology and size highly determine their chemical and physical properties,[11-13] as well as bring the improved catalytic performances. For example, ultrathin Pt network-like nanowires display the enhanced catalytic activity for oxygen reduction reaction, compared with commercial Pt/C catalyst.[14] In another example, hollow PdCu nanoparticles show the improved catalytic activity for formic acid oxidation in comparison with that of solid PdCu nanoparticles.[15]

It is known that Pd catalysts have broad applications in hydrogen storage,[16] gas sensing,[17] and surface-enhanced Raman spectroscopy (SERS),[18] mainly owing to their relatively lower price than Pt catalysts. Particularly, PdM (M = Au, Pt, Cu, and Ag) nanocrystals are the hot research topics because of their synergistic effects and rich diversity of the compositions. Recent reports demonstrate the enhanced catalytic activity of PdM, compared with individual Pd and M (M = Au, Pt, Cu, and Ag) components.[8, 19] Therefore, researchers have prepared a variety of bimetallic PdM nanostructures with different morphology, including hollow PdCu spheres,[20] PdPt concave cubes,[21] PdAu wires,[22] and core-shell Pd@Ag particles.[23]

Recently, much attention is focused on synthesis of dendritic Pd-based nanostructures, because more active sites available on the abundant atomic steps, edges and corners in the dendrites.[24, 25] Lately, dendritic Pd,[3, 24, 25] Pd-Pt,[26, 27] and Pd-Au[28-30] nanostructures are synthesized and widely used as good electrocatalysts in fuel cells.

Oleylamine (OAm) is extensively used for preparation of metallic nanocrystals, due to its multi-roles as the reductant, surfactant, and solvent.[31] However, very few examples about PdM NDs are reported in OAm systems until now, in which complicated synthesis is needed.[32, 33] Therefore, it is still a challenge to develop a facile method to fabricate Pd-based bimetallic NDs.

Herein, a simple one-pot solvothermal route is developed to fabricate PdM NDs (M = Pt, Co, and Ni) by coreduction of Pd (II) acetylacetonate and M (II/III) acetylacetonate. Here, OAm acts as the solvent, reductant, and surfactant, while HDPC serves as a co-surfactant that can further prevent the nanocrystals from aggregation. The electrocatalytic performances of the as-prepared PdM NDs were investigated by cyclic voltammetry and chronoamperometry toward methanol and ethylene glycol oxidation.

2. Experimental section

2.1. Chemicals

Palladium (II) acetylacetonate ($Pd(acac)_2$), platinum (II) acetylacetonate ($Pt(acac)_2$), cobalt (III) acetylacetonate ($Co(acac)_3$), nickel (II) acetylacetonate

($Ni(acac)_2$), oleylamine (OAm), hexadecylpyridinium chloride monohydrate (HDPC), and commercial Pd black catalyst were supplied from Aladdin Chemical Reagent Company (Shanghai, China). Other chemicals were of analytical grade and used without further purification. All the aqueous solutions were prepared with twice-distilled water throughout the whole experiments.

2.2. Synthesis of PdM (M = Pt, Co, and Ni) NDs

For typical preparation of PdM NDs, 0.1 g of HDPC was put into 20 mL of OAm under gentle agitation, and ultrasonicated for 30 min to obtain a homogenous solution. Then, 0.016 g of $Pd(acac)_2$ and 0.020 g of $Pt(acac)_2$ were put into the mixed solution under stirring. After ultrasonication for another 30 min, the mixture was transferred into a Teflon-lined stainless autoclave. The autoclave was kept at 170 °C for 24 h and then allowed to cool to room temperature naturally. The final products were collected and thoroughly washed with ethanol, followed by dispersing the final dispersion in cyclohexane. Similarly, PdCo and PdNi NDs were prepared with $Co(acac)_3$ and $Ni(acac)_2$ instead of $Pt(acac)_2$, respectively, while other conditions were kept unchanged. The concentrations of all the metal precursors are 2.55 mM.

For comparison, individual $Pd(acac)_2$, $Pt(acac)_2$, $Co(acac)_3$, or $Ni(acac)_2$ was used as a precursor to prepared monometallic Pd, Pt, Co, and Ni nanocrystals in a similar way, while other conditions were kept the same.

2.3. Characterization

The morphology and chemical composition of the samples were characterized on a JEM-2100F high resolution transmission electron microscope (HR-TEM) coupled with an energy-dispersive X-ray spectrometer (EDS, Dxford-1NCA) at an acceleration voltage of 200 kV. The scanning transmission electron microscopy (STEM) imaging and elemental mappings were acquired on a scanning transmission electron microscope (STEM) unit with high-angle annular dark-field (HAADF). The oxidation states were determined by a K-Alpha X-ray photoelectron spectrometer (XPS, ThermoFisher, E. Grinstead, UK) with an Al Kα X-ray radiation (1486.6 eV) for excitation. The crystal structure was examined by X-ray diffraction (XRD, Rigaku Dmax-2000 diffractometer) employing Cu Kα radiation.

2.4 Electrochemical measurements

The electrochemical measurements were performed on a CHI832b electrochemical workstation (CH Instruments, Chenhua Co., Shanghai, China) at room temperature. A conventional three-electrode system was employed for all the electrochemical experiments, which includes a Pt mesh as counter electrode, a Ag/AgCl electrode as reference electrode, and a modified glassy carbon electrode (GCE, 3 mm in diameter) as working electrode. All the potentials here were normalized to the reversible hydrogen electrode (RHE).

For construction of PdM (M = Pt, Co, and Ni) NDs modified electrode, 5 mg of the sample was dispersed in 5 mL water by ultrasonication for 60 min to obtain a homogeneous suspension (1.0 mg mL^{-1}). Then, 6 μL of the suspension was dropped onto the electrode surface with a microsyringe. After drying in air, the electrode was further covered with 4 μL of 0.05 wt% Nafion and dried in air. Similarly, home-made Pd NDs and commercial Pd black catalyst modified electrodes were prepared under the same conditions.

CO-stripping voltammetry experiments were performed as follows: CO was bubbled for 15 min to form CO adlayer on the catalyst surface and the working electrode was maintained at –0.1 V. Excess CO in the electrolyte was purged with N_2 for 20 min and CO-stripping voltammograms were recorded via oxidizing pre-adsorbed CO (CO_{ad}) in 0.5 M H_2SO_4 at a scan rate of 50 mV s^{-1}.

To examine the electrocatalytic activity and stability of the as-prepared catalysts, electrochemical experiments were performed by cyclic voltammetry in 1.0 M KOH containing 1.0 M methanol or 0.5 M EG. The current densities in cyclic voltammograms were normalized to electrochemically active surface areas (ECSAs) and loading amount of metals in order to evaluate the catalytic activity.

3. Results and discussion

Morphologies of the typical samples were examined by TEM analysis. Low and high resolution TEM images confirm that the products consist of many uniform and monodisperse NDs, with the average sizes of 51 nm for PdPt (Fig. 1A), 29 nm for PdCo (Fig. 2A), and 32 nm for PdNi (Fig. 3A) dendritic nanostructures, respectively. Importantly, the existence of HDPC was demonstrated essential to form well dispersed PdM NDs, which can effectively prevent the NDs from further aggregation (Fig. S1, Electronic Supplementary Information, ESI). As expected, the absence of HDPC induces the formation of aggregated PdM NDs, verifying the co-stabilizing role of HDPC in the present system.

High-resolution TEM images (insets in Fig.1B, 2B, and 3B) display the associated crystalline fringes of 0.226, 0.225, and 0.224 nm, corresponding to the (111) planes of the face-centered cubic (fcc) PdPt, PdCo, and PdNi alloys, respectively.[33-35] Their polycrystalline nature is clearly manifested by the selected area electron diffraction patterns (SAED) of PdPt (Fig. 1C), PdCo (Fig. 2C), and PdNi (Fig. 3C) NDs, respectively.

Meanwhile, the representative HAADF-STEM images of PdPt, PdCo, and PdNi, along with their elemental mappings for individual elements, verify homogeneous distribution of both Pd and M in each sample, revealing the formation of PdM alloys (Fig. 1D-F, Fig. 2D-F, and Fig. 3D-F). The EDS analysis (Fig. 4) verifies the coexistence of Pd and M elements in the final products. Additionally, the molar ratios of PdPt, PdCo, and PdNi NDs are 86.8/13.2, 77.0/23.0, and 85.0/15.0, respectively.

The alloyed nature of PdM NDs was further proved by XRD analysis (Fig. 5). In all XRD spectra, the diffraction peaks at 40°, 47°, 68°, and 82° are assigned to the (111), (200), (220), and (311) crystal planes of the fcc structure of Pd (JCPDS-46-1043). Clearly, no other distinct diffraction peaks are observed. It indicates that PdM NDs have prevailing fcc Pd crystal structure. The lattice parameters are calculated to be 3.8535 and 3.8642 Å for PdCo and PdNi NDs, based on their corresponding 2θ values of the (111) planes. These values are lower than that of bulk Pd (JCPDS-46-1043, a = 3.8892 Å).[36] The decrease of the lattice parameters and the diffraction characteristics of the fcc Pd structure demonstrate the formation of PdM alloys, reflecting the lattice contraction for partial replacement of Pd by other elements.[37] Besides, the lattice parameter of PdPt NDs is 3.8999 Å, which is higher than that of bulk Pd, but lower than that of bulk Pt (JCPDS-04-0802, a=3.9224 Å).[36] The 2θ values of PdPt diffraction peaks exactly locate between those of the standard Pd and Pt, revealing the formation of PdPt alloys and the substitution of Pd by Pt atoms. Moreover, the average crystallite sizes are 5.7, 3.9, and 3.7 nm for PdPt, PdCo, and PdNi NDs, calculated from the (220) peak based on the Scherrer's equation,[38] respectively.

The surface features of PdM NDs were determined by XPS analysis. Fig. 6 shows the typical high-resolution Pd 3d, Pt 4f, Co 2p, and Ni 2p XPS spectra. The distinct peaks confirm that these atoms do exist in the as-prepared NDs. Meanwhile, for the XPS spectra of PdM NDs, the peaks at 340.5 and 335.5 eV are attributed to the binding energies of Pd $3d_{3/2}$ and Pd $3d_{5/2}$, while there are no obvious peaks from Pd^{2+} observed by fitting these peaks. It means that Pd^{2+} ions are completely reduced to Pd atoms in the present work. However, there are still some Pt^{2+}, Co^{3+}, and Ni^{2+} remained in the final products, by evaluating from the high-resolution Pt 4f, Co 2p, and Ni 2p XPS spectra. Obviously, the incomplete reduction of Co^{3+}, and Ni^{2+} can be due to the lower reduction potential of Co^{3+}/Co (–0.282 V), and Ni^{2+}/Ni (–0.250 V) than that of Pd^{2+}/Pd (0.915 V). However, this reason is not reasonable for explaining the incomplete reduction of Pt^{2+} because of the higher reduction potential of Pt^{2+}/Pt (1.188 V) than that of Pd^{2+}/Pd (0.915 V). Considering that Pt precursor has strong binding affinity to *N*-containing surfactants[39, 40] such as cetyltrimethylamm-onium bromide (CTAB)[13, 41] and cetyltrimethylammonium chloride (CTAC),[42] we postulate that the presence of HDPC would probably affect the reduction rate of Pd species.

For further illustration of the formation mechanism of PdM NDs, single Pd, Pt, Co, and Ni nanoparticles were prepared under the identical conditions (Fig. S2, ESI). TEM image reveals the formation of well-defined Pd NDs, which are different from those of isolated Pt, Co, and Ni monometallic products without any dendrite, owing to the difficult reduction of Pt, Co, and Ni salts.

To better understand the formation mechanism of PdM NDs, the morphological evolution of PdPt was examined as an example at various reaction stages by TEM measurements (Fig. 7). At the initial stage of 30 min (Fig. 7 A), there are a large quantity of tiny particles emerged, with the average diameter of 2~3 nm. With the prolonged reaction time, the pre-generated nanocrystals self-aggregate into immature dendritic nanostructures (Fig. 7 B-C), accompanied with the enlarged particle size. Afterward, immature dendrites gradually and continuously increase until they reach the maximum after 12 h (Fig. 7 D). Further increasing the reaction time (e.g. 24 h, Fig. 1 A) improves the quality of the final products, but without any impact on the particle size. The aggregation-based crystal growth[43] occurs throughout the whole reaction procedure, resulting into high quality of the final products. This is ascribed to the fact that small particles have a higher chemical potential than large ones, because of a larger surface-to-volume ratio.

Based on the above experimental observations, the possible formation mechanism of PdM NDs is described in Fig. 8. Specifically, Pd^{2+} ions are initially reduced to Pd atoms by OAm. At the same time, Pd atoms can absorb M^{n+} ions on their surfaces, and catalyze the reduction of these adsorbed ions.[44] The Pd atoms and the reduced M atoms fuse together, inducing to form tiny PdM nanoclusters, which further aggregate together to form PdM nanoparticles. The as-formed Pd-M nanoparticles self-aggregate to form alloyed PdM NDs by the directing role of OAm.[3, 11, 45]

It is known that hydrogen can diffuse into bulk Pd to form Pd hydride, rather than adsorbing onto Pd surface.[36] Thus, it is not suitable to calculate the ECSAs of a catalyst according to the hydrogen adsorption/desorption strategy. Thus, CO-stripping measurements were usually employed to estimate the ECSAs of the as-prepared catalysts (Fig. 9) based on the following equation (1):[46]

$$\text{ECSAs} = \frac{Q}{m \times C} \qquad (1)$$

where Q is the charge for CO desorption-electrooxidation, m is the loading amount of Pd, and C (420 μC cm^{-2}) is the charge needed for the adsorption of a CO monolayer. The ECSAs are 31.50, 25.52, 22.02, 16.42, and 12.21 m^{2} g^{-1} for PdPt, PdCo, PdNi, Pd NDs, and Pd black catalysts, respectively. The larger ECSAs of PdM NDs and home-made Pd NDs can be ascribed to their interconnected three-dimensional nanostructures. Moreover, the onset potential is 0.64, 0.86, and 0.89 V for PdPt, PdCo, and PdNi NDs, respectively, which are negative than those of home-made Pd NDs

(1.04 V) and Pd black (1.03 V) catalysts. The negative shifts of the onset potentials indicate that PdM NDs have the higher catalytic activity for CO oxidation.

As known, methanol is the most widely used fuel in liquid fuel cells because of its high power density, energy efficiency, capacity, and recyclability.[47] Meanwhile, EG is the most promising fuel for its lower toxicity, low volatility, and high volumetric energy density.[48] Therefore, the electrocatalytic performances of PdM NDs were examined by cyclic voltammetry in 1.0 M KOH containing 1.0 M methanol or 0.5 M EG (Fig. 10).

For methanol oxidation, there are two anodic peaks observed in the forward and reverse scans (Fig. 10A), which correspond to methanol oxidation and the removal of the residual carbonaceous species,[49] respectively. Obviously, the forward anodic peak current densities (j_f) of PdM NDs are higher than those of the Pd NDs and Pd black catalysts modified electrodes. Besides, the onset potentials (E_onset) for PdPt, PdCo, PdNi NDs are –0.085, –0.081, –0.095 V, respectively, which are negative than those on the Pd NDs (–0.079 V) and Pd black (–0.034 V) catalysts modified electrodes. The enhanced catalytic current densities and lower onset potentials suggest the improved catalytic activity of PdM NDs.

Furthermore, the j_f obtained at the peak potentials of these catalysts were normalized to the ECSAs (specific activity) and mass of the metals (mass activity). As shown in table 1, the corresponding specific activities (SA) are 3.34, 2.90, 2.12 mA cm^{-2} for PdPt, PdCo, and PdNi NDs, respectively. These values are larger than Pd NDs (1.31 mA cm^{-2}) and Pd black (0.59 mA cm^{-2}) catalysts. Besides, the mass activities (MA) of the PdPt (1052.33 mA mg^{-1}), PdCo (737.82 mA mg^{-1}), and PdNi (467.36 mA mg^{-1}) NDs modified electrodes are also higher than those of Pd NDs (216.67 mA mg^{-1}) and Pd (71.65 mA mg^{-1}) black catalysts, showing the superior catalytic performances of PdM NDs. Pd black catalyst displays relatively poor catalytic performance, owing to its monometallic, solid spherical (the average diameter is 18.6 nm) properties, and smaller ECSA, as supported by the TEM analysis (Fig. S3, ESI) and CO-stripping data (Fig. 9E). Most importantly, the catalytic activity of PdM NDs is higher, compared with other Pd-based nanostructures reported in the literatures (Table. S1, ESI). A similar trend is found for EG oxidation (see details in Table 1), in which the corresponding j_{f}, E_{onset}, SA, and MA are provided for methanol and EG oxidation.

The stability of the PdM NDs modified electrodes was investigated by chronoamperometry toward methanol (Fig. 11A) and EG (Fig. 11B) oxidation, using Pd NDs and Pd black catalysts as the references. In each case, the corresponding current densities exhibit rapid decays, owing to the formation of CO-like intermediates during methanol and EG oxidation reaction. Impressively, PdM NDs display the enhanced anodic current densities, followed by the much slower decays under the identical conditions, compared with Pd NDs and Pd black catalysts. For example, the specific and mass activity of PdM NDs for methanol (Fig. 11C) and EG oxidation (Fig. 11D) still remain high at 300 s, while those of Pd NDs and Pd black catalysts almost decrease to zero. The enhanced current densities and lagged decays demonstrate the improved electrocatalytic activity, good tolerance to the CO-like intermediates, and long-term stability of PdM NDs.

The improved catalytic performances of PdM NDs over Pd NDs and Pd black catalysts is ascribed to synergistic effects of bimetals.[50] More importantly, the alloyed M can more effectively remove CO-like intermediates adsorbed on Pd active sites via the facile formation of $M(OH)_{ads}$ at a relatively lower potential. As a result, Pd active sites are regenerated, bringing the improved catalytic activity and stability of PdM NDs toward methanol and EG oxidation.

4. Conclusion

In summary, PdM (M = Pt, Co, Ni) NDs have been synthesized in the OAm system by the coreduction of $Pd(acac)_2$ and the corresponding acetylacetonate salts, using HDPC as a stabilizing agent. The control experiments by changing the precursors and reaction time have indicated that the dendritic nanostructures were formed via the aggregation-based crystal growth. The as-prepared PdM nanocrystals exhibited the enhanced electrocatalytic activity and better stability for methanol and EG oxidation, compared with home-made Pd NDs and commercial Pd black catalysts. This is due to their special structures and synergetic effects of Pd with M (M = Pt, Co, Ni). The developed method opens a new route for design and construction of novel Pd-based electrocatalysts in fuel cells.

Acknowledgement

This work was financially supported by the NSFC (Nos. 21175118, 21275130 and 21275131), and Zhejiang province university young academic leaders of academic climbing project (No. pd2013055).

References

1. A. Henglein and M. Giersig, *J. Mater. Chem. B*, 1999, **103**, 9533-9539.
2. T. K. Sau, A. L. Rogach, M. Döblinger and J. Feldmann, *Small*, 2011, **7**, 2188-2194.
3. Q. Gao, M.-R. Gao, J.-W. Liu, M.-Y. Chen, C.-H. Cui, H.-H. Li and S.-H. Yu, *Nanoscale*, 2013, **5**, 3202-3207.
4. H. Bönnemann, N. Waldöfner, H. G. Haubold and T. Vad, *Chem. Mater.*, 2002, **14**, 1115-1120.
5. J. Wu, A. Gross and H. Yang, *Nano Lett.*, 2011, **11**, 798-802.
6. S. Jong Yoo, S.-K. Kim, T.-Y. Jeon, S. Jun Hwang, J.-G. Lee, S.-C. Lee, K.-S. Lee, Y.-H. Cho, Y.-E. Sung and T.-H. Lim, *Chem. Commun.*, 2011, **47**, 11414-11416.
7. L. Deng, W. Hu, H. Deng, S. Xiao and J. Tang, *J. Phys. Chem. C*, 2011, **115**, 11355-11363.
8. V. Mazumder, M. Chi, M. N. Mankin, Y. Liu, Ö. Metin, D. Sun, K. L. More and S. Sun, *Nano Lett.*, 2012, **12**, 1102-1106.
9. Y. Ma, J. Zeng, W. Li, M. McKiernan, Z. Xie and Y. Xia, *Adv. Mater.*, 2010, **22**, 1930-1934.
10. W. Wang, D. Wang, X. Liu, Q. Peng and Y. Li, *Chem. Commun.*, 2013, **49**,

2903-2905.

11. J. Watt, S. Cheong, M. F. Toney, B. Ingham, J. Cookson, P. T. Bishop and R. D. Tilley, *ACS Nano*, 2009, **4**, 396-402.
12. B. Wu, N. Zheng and G. Fu, *Chem. Commun.*, 2011, **47**, 1039-1041.
13. X. Yu, D. Wang, Q. Peng and Y. Li, *Chem. Commun.*, 2011, **47**, 8094-8096.
14. L. Ruan, E. Zhu, Y. Chen, Z. Lin, X. Huang, X. Duan and Y. Huang, *Angew. Chem. Int. Ed.*, 2013, **52**, 12577-12581.
15. L. Yang, C. Hu, J. Wang, Z. Yang, Y. Guo, Z. Bai and K. Wang, *Chem. Commun.*, 2011, **47**, 8581-8583.
16. P. J. Cappillino, J. D. Sugar, M. A. Hekmaty, B. W. Jacobs, V. Stavila, P. G. Kotula, J. M. Chames, N. Y. Yang and D. B. Robinson, *J. Mater. Chem.*, 2012, **22**, 14013-14022.
17. S. Mubeen, T. Zhang, B. Yoo, M. A. Deshusses and N. V. Myung, *J. Phys. Chem. C*, 2007, **111**, 6321-6327.
18. Y. Xiong, J. M. McLellan, J. Chen, Y. Yin, Z.-Y. Li and Y. Xia, *J. Am. Chem. Soc.*, 2005, **127**, 17118-17127.
19. S. Guo, S. Zhang, X. Sun and S. Sun, *J. Am. Chem. Soc.*, 2011, **133**, 15354-15357.
20. C. Hu, Y. Guo, J. Wang, L. Yang, Z. Yang, Z. Bai, J. Zhang, K. Wang and K. Jiang, *ACS Appl. Mat. Interfaces*, 2012, **4**, 4461-4464.
21. H. Zhang, M. Jin, J. Wang, W. Li, P. H. C. Camargo, M. J. Kim, D. Yang, Z. Xie and Y. Xia, *J. Am. Chem. Soc.*, 2011, **133**, 6078-6089.
22. C. Zhu, S. Guo and S. Dong, *Adv. Mater.*, 2012, **24**, 2326-2331.

23. J. Gong, F. Zhou, Z. Li and Z. Tang, *Chem. Commun.*, 2013, **49**, 4379-4381.
24. S. Patra, B. Viswanath, K. Barai, N. Ravishankar and N. Munichandraiah, *ACS Appl. Mat. Interfaces*, 2010, **2**, 2965-2969.
25. A.-J. Wang, F.-F. Li, Z. Bai and J.-J. Feng, *Electrochim. Acta*, 2012, **85**, 685-692.
26. X. Chen, Z. Cai, X. Chen and M. Oyama, *J. Mater. Chem. A*, 2014, **2**, 315-320.
27. L. Wang and Y. Yamauchi, *Chem. Asian*, 2010, **5**, 2493-2498.
28. H. Ataee-Esfahani, L. Wang and Y. Yamauchi, *Chem. Commun.*, 2010, **46**, 3684-3686.
29. R. Huang, Y.-H. Wen, G.-F. Shao, Z.-Z. Zhu and S.-G. Sun, *J. Phys. Chem. C*, 2013, **117**, 6896-6903.
30. L. Kuai, X. Yu, S. Wang, Y. Sang and B. Geng, *Langmuir*, 2012, **28**, 7168-7173.
31. S. Mourdikoudis and L. M. Liz-Marzán, *Chem. Mater.*, 2013, **25**, 1465-1476.
32. Z. Peng and H. Yang, *J. Am. Chem. Soc.*, 2009, **131**, 7542-7543.
33. P. Xi, Y. Cao, F. Yang, C. Ma, F. Chen, S. Yu, S. Wang, Z. Zeng and X. Zhang, *Nanoscale*, 2013, **5**, 6124-6130.
34. X. Huang, Y. Li, Y. Li, H. Zhou, X. Duan and Y. Huang, *Nano Lett.*, 2012, **12**, 4265-4270.
35. C. Xu, Y. Liu, Q. Hao and H. Duan, *J. Mater. Chem. A*, 2013, **1**, 13542-13548.
36. S.-S. Li, J.-J. Lv, Y.-Y. Hu, J.-N. Zheng, J.-R. Chen, A.-J. Wang and J.-J. Feng, *J. Power Sources*, 2014, **247**, 213-218.
37. S. Mukerjee, S. Srinivasan, M. P. Soriaga and J. McBreen, *J. Phys. Chem.*, 1995, **99**, 4577-4589.

38. C. Venkateswara Rao, C. R. Cabrera and Y. Ishikawa, *J. Phys. Chem. C*, 2011, **115**, 21963-21970.

39. M. Grote, U. Hüppe and A. Kettrup, *Talanta*, 1984, **31**, 755-762.

40. L. D'Souz and S. Sampath, *Langmuir*, 2000, **16**, 8510-8517.

41. B. Y. Xia, H. B. Wu, X. Wang and X. W. Lou, *J. Am. Chem. Soc.*, 2012, **134**, 13934-13937.

42. S. W. Kang, Y. W. Lee, Y. Park, B.-S. Choi, J. W. Hong, K.-H. Park and S. W. Han, *ACS Nano*, 2013, **7**, 7945-7955.

43. B. Lim and Y. Xia, *Angew. Chem. Int. Ed.*, 2011, **50**, 76-85.

44. D. Wang and Y. Li, *J. Am. Chem. Soc.*, 2010, **132**, 6280-6281.

45. Z. Yin, H. Zheng, D. Ma and X. Bao, *J. Phys. Chem. C*, 2008, **113**, 1001-1005.

46. S.-S. Li, Y.-Y. Hu, J.-J. Feng, Z.-Y. Lv, J.-R. Chen and A.-J. Wang, *Int. J. Hydrogen Energy*, 2014, **39**, 3730-3738.

47. Y. Lu, Y. Jiang, H. Wu and W. Chen, *J. Phys. Chem. C*, 2013, **117**, 2926-2938.

48. J.-N. Zheng, J.-J. Lv, S.-S. Li, M.-W. Xue, A.-J. Wang and J.-J. Feng, *J. Mater. Chem. A*, 2014, **2**, 3445-3451.

49. J.-N. Zheng, S.-S. Li, X. Ma, F.-Y. Chen, A.-J. Wang, J. Chen and J.-J. Feng, *J. Mater. Chem. A*, 2014, **2**, 8386-8395.

50. A. K. Singh and Q. Xu, *ChemCatChem*, 2013, **5**, 652-676.

Captions

Fig. 1. (A, B) TEM images, (C) SEAD pattern, (D) HAADF-STEM images, and (E, F) EDS mapping of PdPt NDs. Insets show the corresponding size distribution in (A) and HRTEM image in (B).

Fig. 2. (A, B) TEM images, (C) SEAD pattern, (D) HAADF-STEM images, and (E, F) EDS mapping of PdCo NDs. Insets show the corresponding size distribution in (A) and HRTEM in (B).

Fig. 3. (A, B) TEM images, (C) SEAD pattern, (D) HAADF-STEM images, and (E, F) EDS mapping of PdNi NDs. Insets show the corresponding size distribution in (A) and the HRTEM image in (B).

Fig. 4. EDS patterns of (A) PdPt, (B) PdCo, and (C) PdNi NDs.

Fig. 5. XRD patterns of PdPt, PdCo, and PdNi NDs. For comparison, bulk Pd, Pt, Co, and Ni from JCPDS were also included.

Fig. 6. High-resolution XPS spectra of Pt 4f, Co 2p, Ni 2p, and Pd 3d in PdM NDs.

Fig. 7. TEM images of PdPt products obtained at different time intervals: (A) 30 min, (B) 1 h, (C) 6 h, and (D) 12 h.

Fig. 8. The possible formation mechanism of PdM NDs.

Fig. 9 CO-stripping voltammograms of (A) PdPt, (B) PdCo, (C) PdNi, (D) Pd NDs, and (E) Pd black catalysts in 0.5 M H_2SO_4 with the scan rate of 50 mV s^{-1}.

Fig. 10. Cyclic voltammograms of the PdM NDs, home-made Pd and Pd black catalysts modified electrodes in (A) 1.0 M KOH + 1.0 M methanol and (B) 1.0 M KOH + 0.5 M EG at a scan rate of 50 mV s^{-1}.

Fig. 11. Chronoamperometric curves of the PdM NDs, home-made Pd and Pt black catalysts modified electrodes in (A) 1.0 M KOH + 1.0 M methanol and (B) 1.0 M KOH + 0.5 M EG by applying a potential of 0.15 V (*vs*. RHE). The corresponding specific activity and mass activity for (C) methanol and (D) EG oxidaition obtained at 300 s.

Table 1. Comparison of the electrocatalytic activity of the PdM NDs, Pd NDs, and commercial Pd black catalysts modified electrodes for methanol and EG oxidation.

Figures

Fig. 1

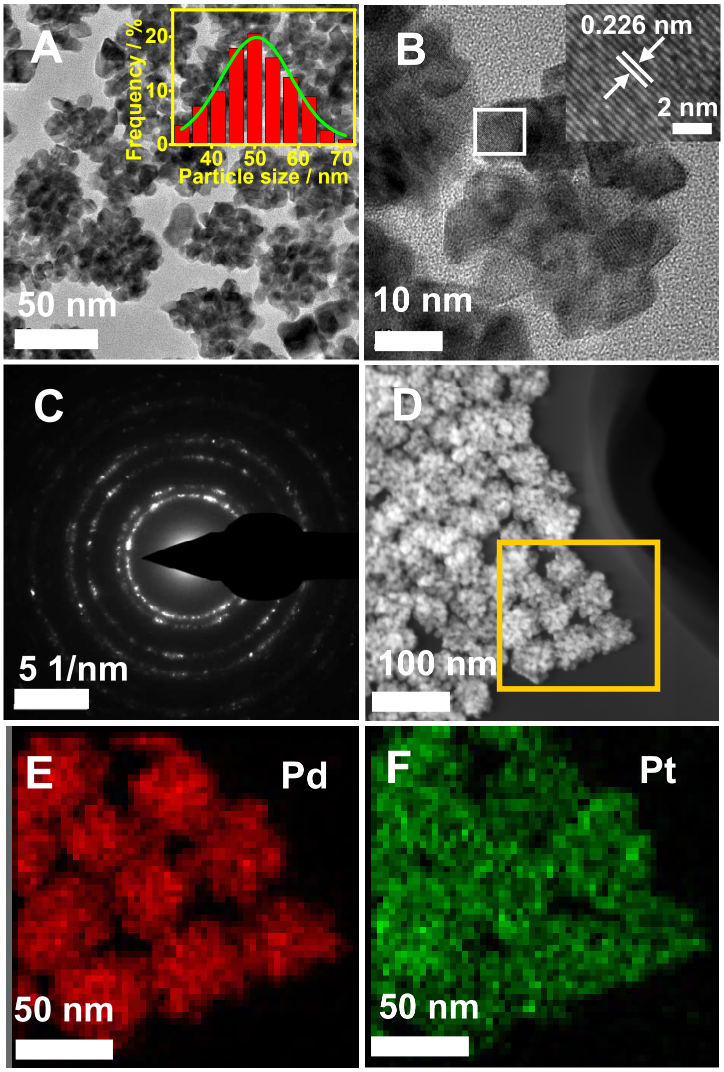

Fig. 2

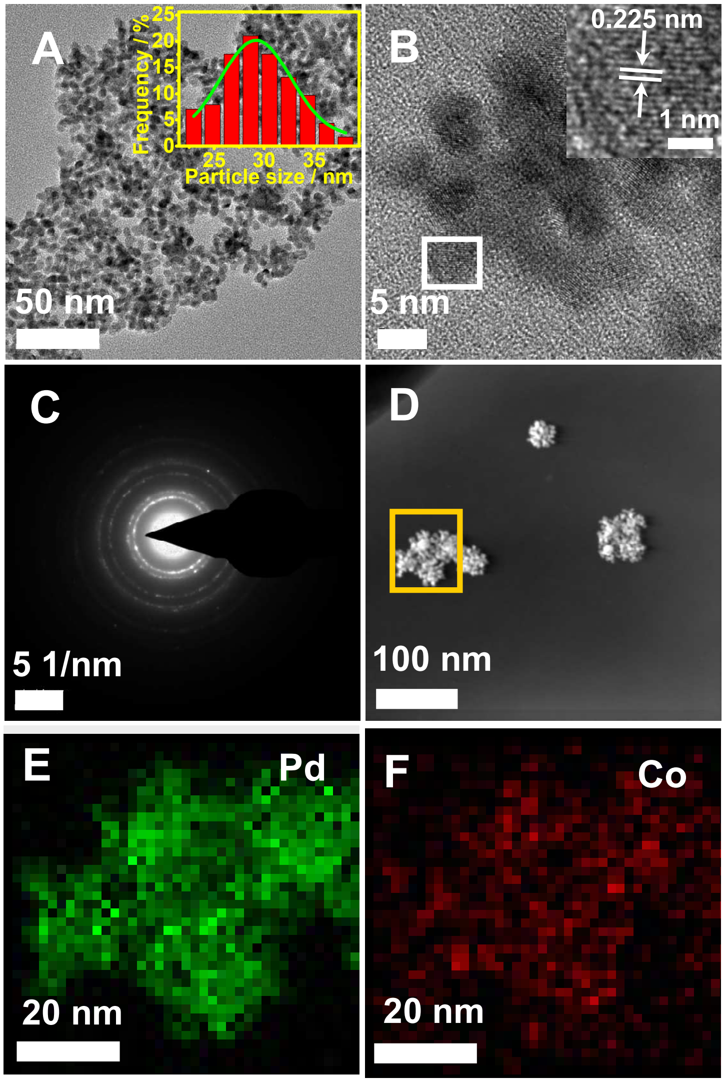
A
Frequency / %
25
20
15
10
5
0
25
30
35
Particle size / nm
50 nm
B
0.225 nm
1 nm
5 nm
C
5 1/nm
D
100 nm
E
Pd
20 nm
F
Co
20 nm

Fig. 3

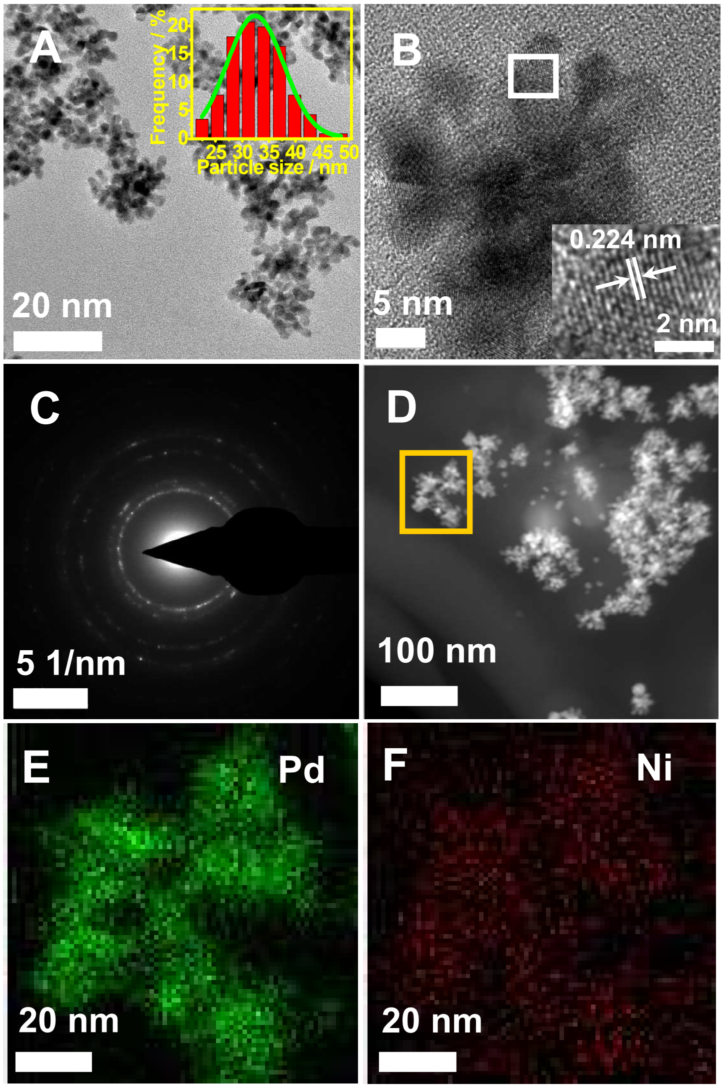
A
Frequency / %
0
5
10
15
20
25 30 35 40 45 50
Particle size / nm
20 nm
B
0.224 nm
5 nm
2 nm
C
5 1/nm
D
100 nm
E
Pd
20 nm
F
Ni
20 nm

Fig. 4

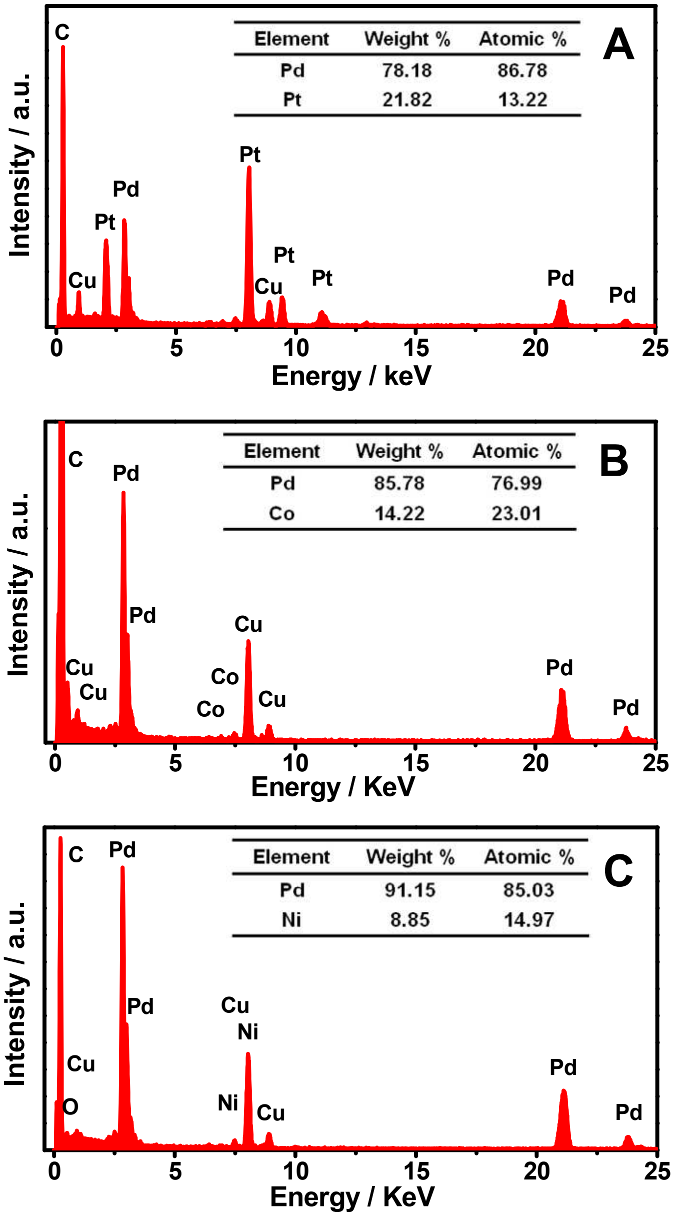

A

Element	Weight %	Atomic %
Pd	78.18	86.78
Pt	21.82	13.22

B

Element	Weight %	Atomic %
Pd	85.78	76.99
Co	14.22	23.01

C

Element	Weight %	Atomic %
Pd	91.15	85.03
Ni	8.85	14.97

Fig. 5

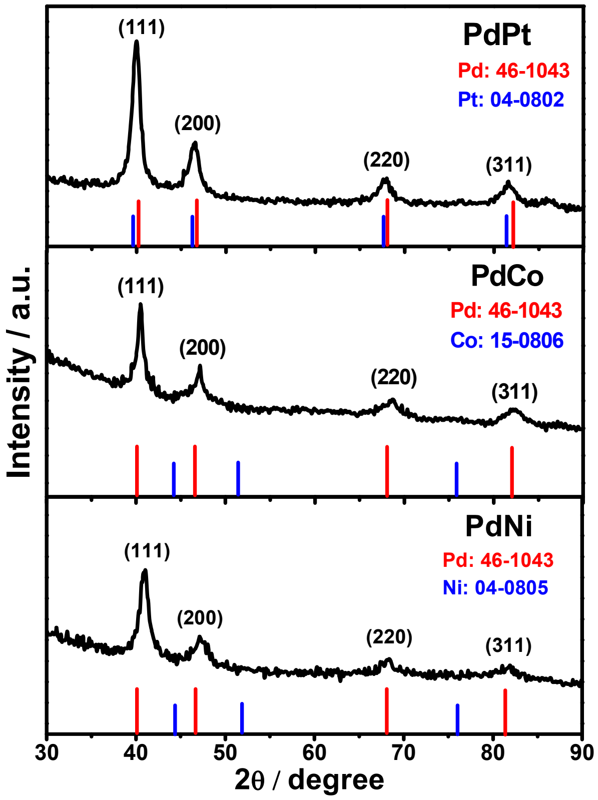
PdPt
Pd: 46-1043
Pt: 04-0802
PdCo
Pd: 46-1043
Co: 15-0806
PdNi
Pd: 46-1043
Ni: 04-0805
(111)
(200)
(220)
(311)
Intensity / a.u.
2θ / degree
30
40
50
60
70
80
90

Fig. 6

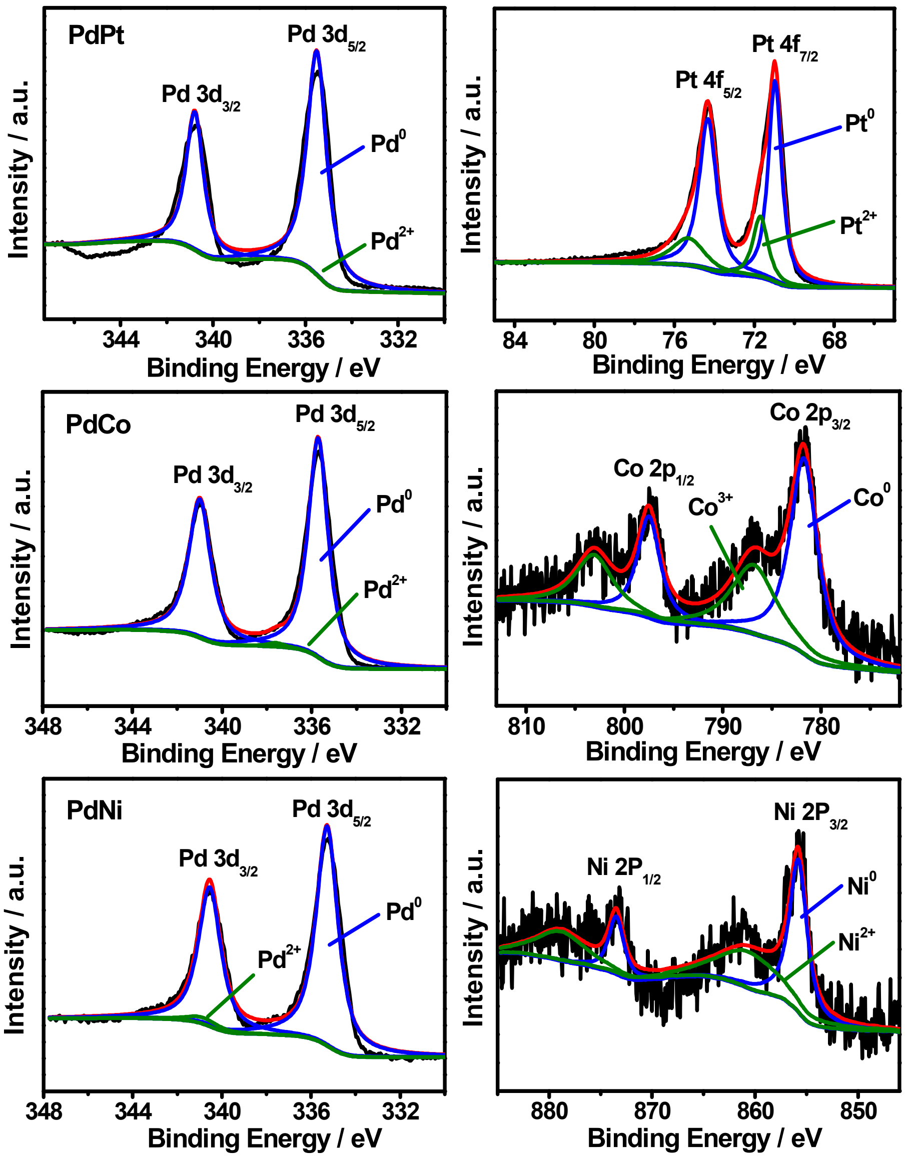
PdPt
Pd 3d$_{5/2}$
Pd 3d$_{3/2}$
Pd^0
Pd^{2+}
Intensity / a.u.
344 340 336 332
Binding Energy / eV
Pt 4f$_{7/2}$
Pt 4f$_{5/2}$
Pt^0
Pt^{2+}
Intensity / a.u.
84 80 76 72 68
Binding Energy / eV
PdCo
Pd 3d$_{5/2}$
Pd 3d$_{3/2}$
Pd^0
Pd^{2+}
Intensity / a.u.
348 344 340 336 332
Binding Energy / eV
Co 2p$_{3/2}$
Co 2p$_{1/2}$
Co^{3+}
Co^0
Intensity / a.u.
810 800 790 780
Binding Energy / eV
PdNi
Pd 3d$_{5/2}$
Pd 3d$_{3/2}$
Pd^0
Pd^{2+}
Intensity / a.u.
348 344 340 336 332
Binding Energy / eV
Ni 2P$_{3/2}$
Ni 2P$_{1/2}$
Ni^0
Ni^{2+}
Intensity / a.u.
880 870 860 850
Binding Energy / eV

Fig. 7

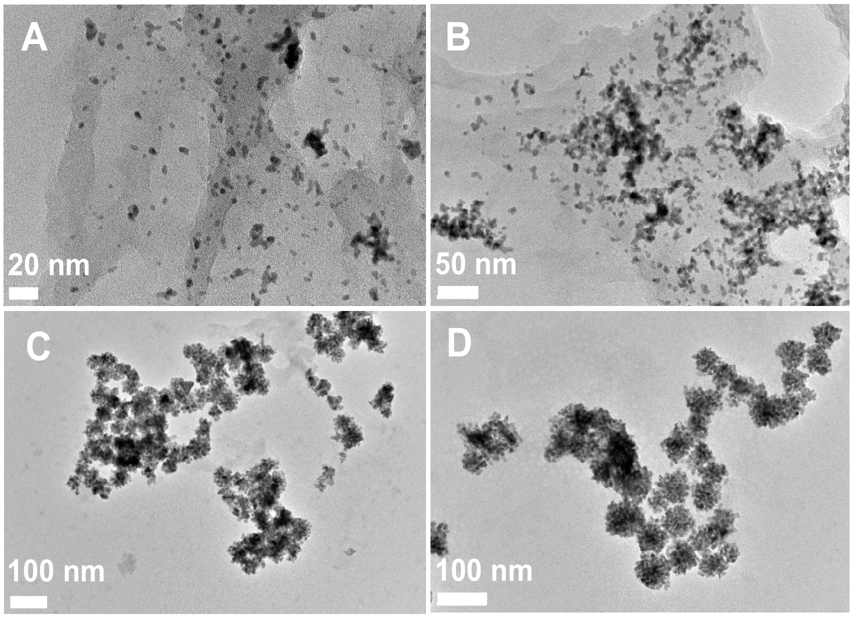

Fig. 8

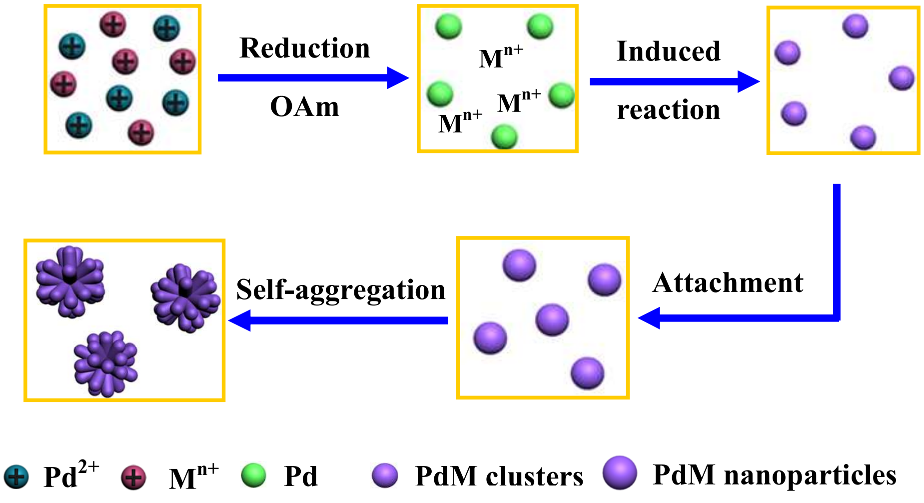
Reduction
OAm
M^{n+}
M^{n+}
M^{n+}
Induced
reaction
Attachment
Self-aggregation
Pd^{2+}
M^{n+}
Pd
PdM clusters
PdM nanoparticles

Fig. 9

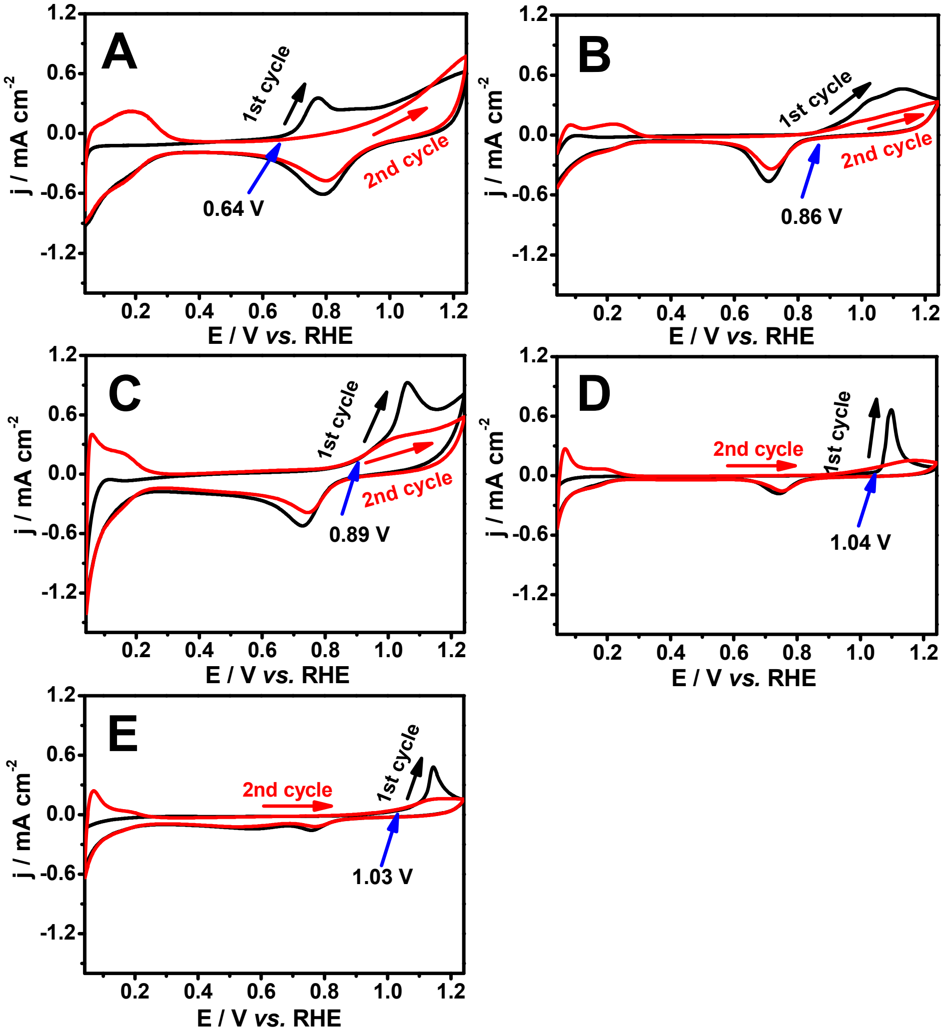
A
1st cycle
2nd cycle
0.64 V
B
1st cycle
2nd cycle
0.86 V
C
1st cycle
2nd cycle
0.89 V
D
2nd cycle
1st cycle
1.04 V
E
2nd cycle
1st cycle
1.03 V
j / mA cm-2
E / V vs. RHE
1.2
0.6
0.0
-0.6
-1.2
0.2
0.4
0.6
0.8
1.0
1.2

Fig. 10

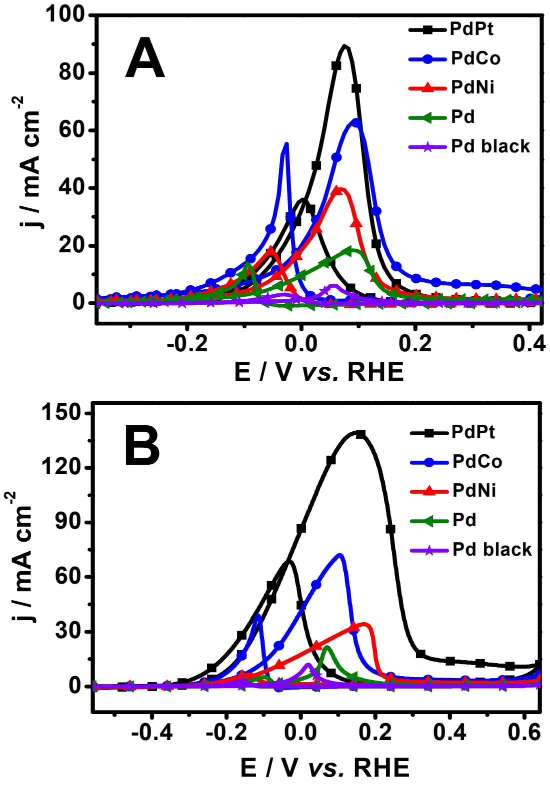
A
100
80
60
40
20
0
j / mA cm^{-2}
-0.2
0.0
0.2
0.4
E / V *vs.* RHE
PdPt
PdCo
PdNi
Pd
Pd black
B
150
120
90
60
30
0
j / mA cm^{-2}
-0.4
-0.2
0.0
0.2
0.4
0.6
E / V *vs.* RHE
PdPt
PdCo
PdNi
Pd
Pd black

Fig. 11

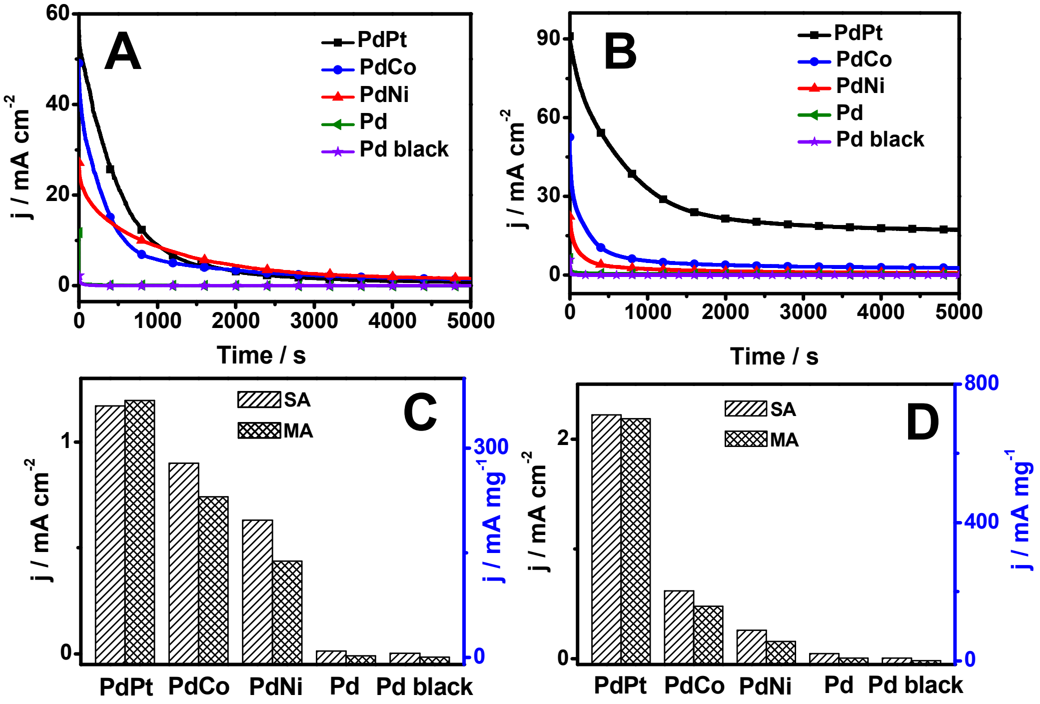
A
B
C
D
PdPt
PdCo
PdNi
Pd
Pd black
j / mA cm^{-2}
Time / s
0
20
40
60
30
90
1000
2000
3000
4000
5000
SA
MA
j / mA mg^{-1}
1
2
300
400
800

Table 1

Catalysts	j_f/mA cm^{-2}	E_{onset}/V	SA/mA cm^{-2}	MA/mA mg^{-2}
PdPt	89.37 (methanol)	–0.085 (methanol)	3.34 (methanol)	1052.33 (methanol)
	139.02 (EG)	–0.204 (EG)	5.20 (EG)	1638.3 (EG)
PdCo	62.22 (methanol)	–0.081 (methanol)	2.90 (methanol)	737.82 (methanol)
	72.03 (EG)	–0.161 (EG)	3.33 (EG)	850.0 (EG)
PdNi	39.69 (methanol)	–0.095 (methanol)	2.12 (methanol)	467.36 (methanol)
	33.97 (EG)	–0.199 (EG)	1.83 (EG)	401.67 (EG)
Pd	18.41 (methanol)	–0.079 (methanol)	1.31 (methanol)	216.67 (methanol)
	21.37 (EG)	–0.046 (EG)	1.53 (EG)	251.66 (EG)
Pd black	6.03 (methanol)	–0.034 (methanol)	0.59 (methanol)	71.65 (methanol)
	11.84 (EG)	–0.097 (EG)	1.15 (EG)	140.0 (EG)

Graphical Abstract

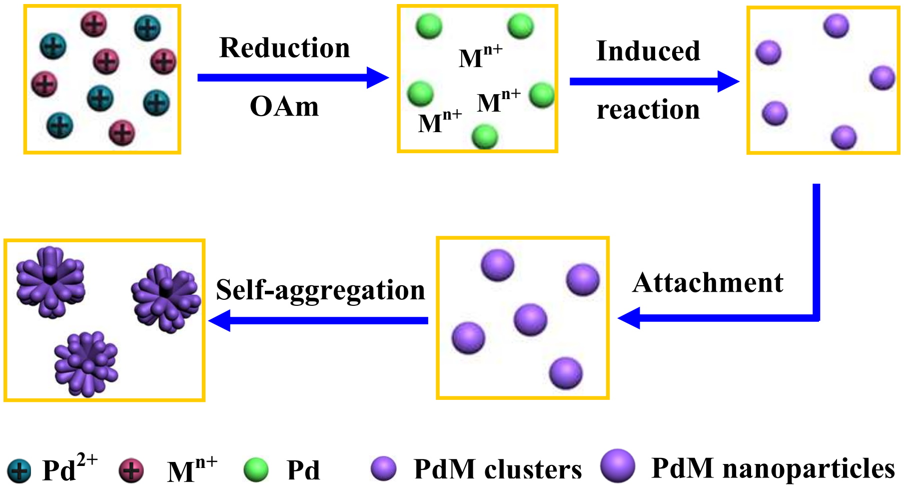

PdM (M = Pt, Co, and Ni) nanodendrites were fabricated by a co-reduction strategy. The nanodendrites displayed the enhanced catalytic activities and stabilities for methanol and ethylene glycol oxidation.